Macroscopic Orientation Domains Grown via Aerodynamic Levitation: A Path toward Single Crystals

Wolfgang Wisniewski, Michael J Pitcher, Emmanuel Veron, Jintai Fan, Vincent Sarou-Kanian, Franck Fayon, Mathieu Allix

Macroscopic Orientation Domains grown via Aerodynamic Levitation - a Path towards Single Crystals

WolfgangWisniewski[1,2], Michael J. Pitcher[1], Emmanuel Veron[1], Jintai Fan[1,3], Vincent Sarou-Kanian[1], Franck Fayon[1] and Mathieu Allix[1]*

[1]CNRS, CEMHTI UPR3079, Univ. Orléans, F-45071 Orléans, France.

[2]Le Studium Research Fellow, Loire Valley Institute for Advanced Studies, Orléans & Tours, France.

[3]Chinese Academy of Science, Shanghai Institute of Optics and Fine Mechanics, Shanghai 201800, P. R. China.

Keywords: $La_2Ga_3O_{7.5}$, aerodynamic levitation, EBSD, flash crystallization,

*Corresponding Author: Wolfgang Wisniewski wolfgang.w@uni-jena.de

Abstract

Powder pellets of ca. 30 mg with the mol% composition $0.61Ga_2O_30.39La_2O_3$ are levitated in a gas stream and melted using a pair of CO_2 lasers. The levitating melt droplets crystallize to form $La_2Ga_3O_{7.5}$ or $LaGaO_3$ after the lasers are turned off. The microstructure of cross sections prepared from them is analyzed using scanning electron microscopy (SEM) and electron backscatter diffraction (EBSD).

One of the beads containing $La_2Ga_3O_{7.5}$ shows a fully crystallized, polycrystalline microstructure while the other broke apart during cooling and its cross section shows only a single orientation domain which is more than 7 mm^2 in area. Solid-state ^{71}Ga NMR spectroscopy was applied to this sample and showed that it was not a single crystal but contains

only about 3 orientation domains. The bead containing $LaGaO_3$ showed dendritic growth originating from multiple nuclei.

Although a single crystal was not achieved by the applied experiments so far, a detailed correlation of measured cooling curves with the observed microstructures enables to devise steps along the path towards single crystal production in future experiments.

1. Introduction

Crystallization in spheres of glass or melt droplets can occur via various mechanisms and hence show a wide range of morphologies. Glasses free of nucleation agents often nucleate at the surface, sometimes showing oriented nucleation [1], which is often followed by bulk nucleation after some time. A complete bulk nucleation is also possible when high nucleation rates occur as e.g. reported for glasses with the stoichiometric composition of Ba-fresnoite [2,3]. The subsequent crystal growth in such glasses depends on a wide range of parameters. Microspheres produced via flame synthesis have been shown to crystallize via multiple growth mechanisms from slow growing polygon grains to fast growing dendrites, sometimes showing mechanism changes within a sphere or phase separation before the crystallization event [4].

While the process of flame synthesis [5] enables to screen the range of possible crystallization routes in melts of a chosen composition range [4] by producing a huge number of small spheres subjected to a range of experimental conditions, the process of levitation melting enables much larger spheres exposed to a somewhat more controllable environment while still avoiding contact to a solid or liquid interface, i.e. containerless melting [6-8], which allows extreme undercooling temperatures [8]. This enables to synthesize non-equilibrium phases that are difficult to produce via more classic preparation methods.

Applying aerodynamic levitation to several compositions in the xLa_2O_3-$(100-x)Ga_2O_3$ system found the glass-forming region to be $20 \leq x \leq 57$ and these glasses have been proposed as attractive host materials due to their optical properties [9]. A phase with the composition $La_2Ga_3O_{7.5}$ can be crystallized from such melts; it is the end member of a group of oxide ion conducting layered melilite materials with the composition $La_{1+x}Sr_{1-x}Ga_3O_{7+x/2}$, i.e. with x=1, and contains interstitial oxide defects that are fully ordered into chains within the $Ga_3O_{7.5}$ layers [12]. $La_2Ga_3O_{7.5}$ is metastable, with a decomposition temperature of 830°C [12], and cannot be prepared by a conventional high temperature ceramic reaction so far.

Materials composed of compounds with the general composition $La_{1+x}Sr_{1-x}Ga_3O_{7+x/2}$ are of interest for solid oxide fuel cell (SOFC) applications due to their anionic, non-stoichiometry inducing oxide ion conductivity [10-12]. Due to very thin grain boundaries and the limited birefringence of their melilite structure, these materials can also show a certain transparency when produced via levitation melting [11-13]. They also show a high refractive index due to the heavy elements in the composition and the optical emissions can be easily modified by substituting La with rare earth elements, giving rise to optical emissions to allow e.g. luminescent and/or scintillating functions [13].

The transparency of these materials is essential for optical applications, but currently the process sometimes requires several steps of re-melting (e.g. to remove excess Ga_2O_3) [12] to produce transparent, crystalline beads. In this manuscript, the growth mechanisms in beads produced via aerodynamic levitation are analyzed in order to gain insight into why some beads are opaque while others are transparent. The observed growth mechanisms enable to draw conclusions concerning the experimental conditions during crystallization and hence propose process modifications to maximize the desired outcome.

2. Materials and methods

Crystallized beads were obtained from batches of the nominal mol% composition $0.61Ga_2O_3 \bullet 0.39La_2O_3$ using two melt-quenching protocols. The excess Ga_2O_3 (compared to the target composition $La_2Ga_3O_{7.5}$) is required to compensate for vaporization during melting. Protocol 1 was reported in detail in Ref. [12]: La_2O_3 and Ga_2O_3 powders were weighed and then mixed in an agate mortar using an ethanol suspension, dried at 100 °C and then pressed into pellets using a uniaxial pressure of 20 MPa. Pellet fragments weighing ca. 30 mg were placed into the conical nozzle of the aerodynamic levitator system where they were heated by a pair of CO_2 lasers while levitating in a flow of oxygen gas. The sample temperature was monitored by a monochromatic pyrometer ($\lambda = 0.8$ μm).

Cooling curves of pure Al_2O_3 melts were recorded and evaluated to estimate the true temperature measured by the uncalibrated pyrometer, they are available in the supplemental material. Cooling was achieved by turning the laser off or linearly decreasing the laser power over times of 10, 60 or 120s. The corresponding maximum temperatures measured for the crystallization peaks are 1945, 1962, 1974 and 1977 °C, respectively. Considering that a melt cannot be heated above the melting point T_m of the crystallizing phase by the released crystallization energy, it is plausible to assume the true temperature in the samples was below the T_m of Al_2O_3 at 2054 ± 6°C [14]. Assuming the measured valued of 1977 °C actually represents the T_m of Al_2O_3, this would mean a maximum deviation of 83 K. In reality, the deviation should be less because the melted Al_2O_3 powder was not of extreme purity and the crystal growth rates approach zero as the temperature approaches T_m.

Considering this possible deviation, melting of the prepared beads visible to the naked eye was observed above approximately 1700 °C, after which the samples were heated by another 150 K for several seconds to homogenize the melt at the homogenization temperature T_{hom}. After cooling the melt spheres by ca. 300 K the lasers were switched off, allowing the samples to cool to room temperature in the oxygen gas stream. Protocol 2 was applied to comparably produced reaction pellets but with argon as the levitation gas. As in protocol 1, the melt was prepared at above ca. 1700 °C before raising the temperature by 150 K. After several seconds, the lasers were switched off, allowing the melt to cool directly to room temperature.

Selected beads were embedded in Araldite 2020 and ground to prepare cross sections for microstructure analyses. These cross sections were polished with abrasive slurries down to a diamond paste of 1 µm grain size. A final finish of 4 h vibration polishing using the PRESI super finish (0.03 µm) on a Buehler VibroMet 2 was applied. All samples were contacted with Ag-paste and coated with a thin layer of carbon to avoid surface charging in the SEM.

The microstructure was analyzed using scanning electron microscopy (SEM) using a TESCAN MIRA 3 XMU equipped with an EDAX Pegasus system system. Energy-dispersive X-ray spectroscopy (EDXS) was performed without a standard using an acceleration voltage of 20 kV which was also used for EBSD-scans. They were captured and evaluated using the software TSL OIM Data Collection 7 and TSL OIM Analysis 7. Pseudo symmetry cleanups (a 180° rotation of the (112) plane for $GaLaO_3$ and a 90° rotation of the (100) plane for $Ga_3La_2O_{7.5}$) were applied. Unreliable data points were removed by applying a Confidence Index (CI) filter of 0.1 after performing a grain CI standardization.

Solid-state ^{71}Ga NMR spectroscopy was performed with a Bruker Avance III HD spectrometer operating with a 17.6 T magnet (^{71}Ga Larmor frequency of 228.76 MHz) and a 3.2 mm rotor.

NMR spectra in static conditions were recorded using a spin echo experiment (echo delay of 20 µs, a radio-frequency field of ca. 86 kHz, recycling delay of 0.5 s, 512 accumulations) with a Bruker magic angle spinning (MAS) probehead. The rotor was spun at ~1 Hz and the acquisition was synchronized with the rotor pitch in order to obtain static spectra for 180 rotor pitches with a variation of 1°. "Static" conditions refers to a duration of the free induction decay being less than 600 µs while the sample rotated along the MAS axis for less than 1°.

3. Results and Discussion

Aerodynamic levitation melting and the subsequent cooling, which occurs with about 300 K/s, leads to beads which either appear transparent or opaque. Figure 1 shows optical micrographs of cross sections through such beads prepared for SEM-analysis that appear a), b) transparent or c) opaque to the naked eye. The beads in Figure 1 a) and c) were produced using protocol 2 while the bead in Figure 1 b) was prepared using protocol 1. Silver paste from the preparation for SEM appears bright.

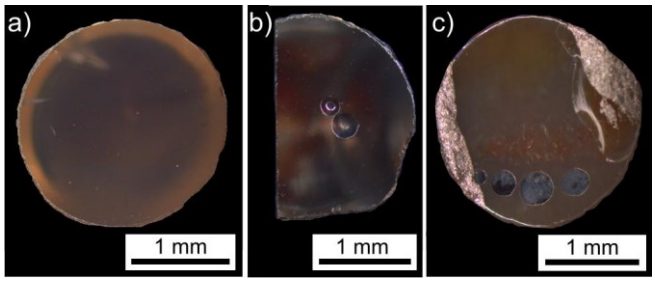

Figure 1: Optical dark field micrographs of cross sections through beads prepared for SEM analysis. They appear a), b) transparent to the naked eye or c) opaque.

Temperature curves recorded while cooling beads to achieve the results featured in Figure 1 are presented in Figure 2. The temperature spike during cooling can be attributed to the exothermal release of the crystallization energy and hence should not be observed if a glassy bead is formed. Curve a) includes quenching from a plateau 300 K below T_{hom} and shows the most discreet temperature spike, indicating the fastest crystallization and subsequent cooling

of the bead. Curve b) is the result of quenching from T_{hom} and shows a broader spike which is slightly broader in curve c) resulting from the same protocol but an opaque sample.

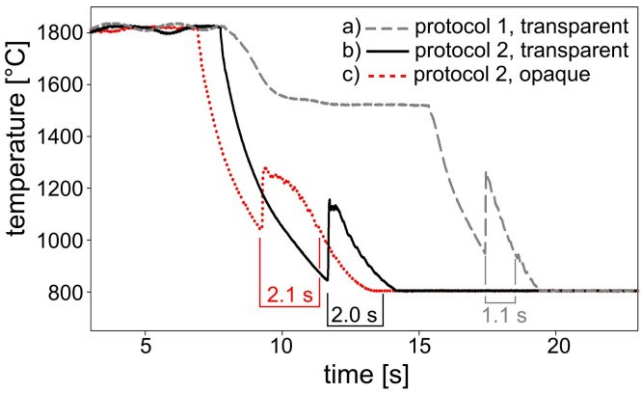

Figure 2: Relative temperatures recorded while cooling the levitating beads from T_{hom} leading to the respectively stated results. The bottom temperature plateau results from the detection limit of the pyrometer. The temperature values assume no difference in emissivity between the beads or between the solid/liquid phases.

Relevant parameters of the crystallization peaks in Figure 2 are presented in Table 1. The curves a) and b) show a similar temperature increase during crystallization, but it is reached more than twice as fast as in curve a) which also shows a much shorter crystallization peak altogether. Curve c) shows a much slower temperature increase which stops at ca. $2/3^{ds}$ of the temperature increase of the curves a) and b). Despite the smaller temperature increase, this bead took even longer to cool back to the temperature where crystallization began.

Table 1: Time and temperature differences for the exothermic peaks of the curves a-c) in Figure 2: The duration of the initial temperature increase Δt (exo), the maximum temperature increase ΔT (exo) and the full time until the starting temperature of the crystallization peak is reached again Δt (peak).

	Δt (exo) [s]	**ΔT (exo) [°K]**	**Δt (peak) [s]**
curve a)	0.036	318	1.107
curve b)	0.090	312	2.007
curve c)	0.177	244	2.163

An SEM-micrograph of the transparent sample featured in Figure 1 a) is presented in Figure 3 a). It implies polycrystalline crystallization and a chemical at% composition of

23.5 Ga • 16.5 La • 60.0 O was determined over 15 EDXS spot measurements. The composition was homogenous at all spots within the margin of error and is in acceptable agreement with the ideal composition of $La_2Ga_3O_{7.5}$, hence a material file based on Ref. [12] was used during the subsequent EBSD analysis.

The image quality (IQ)-maps of EBSD-scans performed on this cross section presented in Figure 3 b) indicate a wide range of EBSD-pattern qualities obtainable from this sample. The EBSD-patterns 1-3 were acquired at the locations 1-3. Pattern 1 represents the high pattern quality obtainable from some areas. Pattern 2 originates from an area where a clear grain structure is not discernible: it shows signs of EBSD-pattern superposition, implying that the orientation domains in this area are probably so small that this region fails to provide high quality EBSD-patterns allthough it is fully crystallized. EBSD pattern 3 does not show any clear Kikuchi lines and hence could result from uncrystallized glass or a microstructure unsuited to allow electron diffraction as e.g. also observed during the crystallization of diopside [15] or $BaTiO_3$ [16]. The inverse pole figure (IPF)+IQ-map in Figure 3 c) confirms the varying grain sized and the orientational homogeneity within the grains, i.e. independent nucleation for each discernible grain.

The grain size increases towards the center/left side of the sample, indicating nucleation occurred in a thermal gradient: high nucleation rates near the cooler surface of the sphere but less nuclei near the center accompanied by faster crystal growth due to higher temperatures. The transparency of comparable polycrystalline melilite ceramics with such large grains of non-cubic symmetry is caused by the low birefringence and thin grain boundaries form by this phase [11].

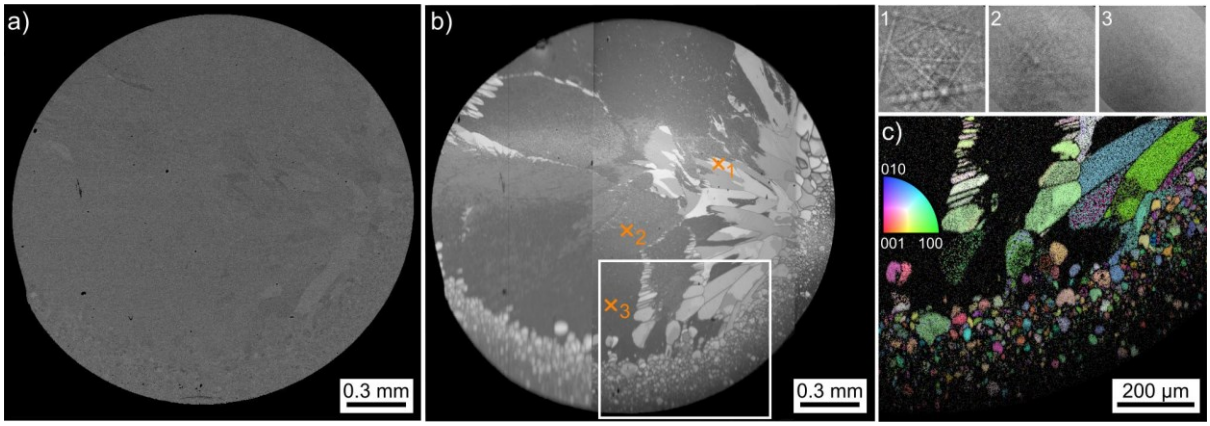

Figure 3: Electron microscopy results of the bead featured in Figure 1 a): a) SEM micrograph of the cross section, b) IQ-maps of EBSD-scans performed on this cross section and c) IPF+IQ-map of the framed area. The EBSD-patterns 1-3 were acquired at the locations 1-3.

The sample presented in Figure 1 b) was synthesized using protocol 1 and is a segment of a bead that broke during cooling. Figure 4 a) shows an SEM-micrograph of a cross section through the transparent bead segment more than 7 mm^2 in area and containing two large pores. 10 EDXS-spot measurements were acquired from this cross section show the average at% composition, neglecting possible contaminants, to be 23.9 Ga • 16.2 La • 60.0 O, i.e. a good agreement with the ideal composition of $La_2Ga_3O_{7.5}$. Figure 4 b) shows the orientation+IQ-map of an EBSD-scan performed on the bead, illustrating that all EBSD-patterns deviate less than 3° from the stated orientation. The parallel lines highlighted by the white arrow originate from slightly different EBSD-patterns, but crystallographic twinning could not be verified so it is likely that they originate from a local contamination or stresses.

While this information is of course limited to the analyzed cross section and the significant information depth of EBSD is less than 100 nm for most measurements [17], it is quite possible that the entire bead/segment crystallized from a single nucleus, forming a single crystal large enough to measure various properties. On the other hand, the fact that the bead broke spontaneously during cooling indicates that the initial bead was probably composed of a few, very large orientation domains, possibly resulting from a countable number of nucleation events. During cooling, the coefficients of thermal expansion along differing crystallographic

directions would lead to stresses amongst the large grains, possibly causing them to fracture along grain boundaries.

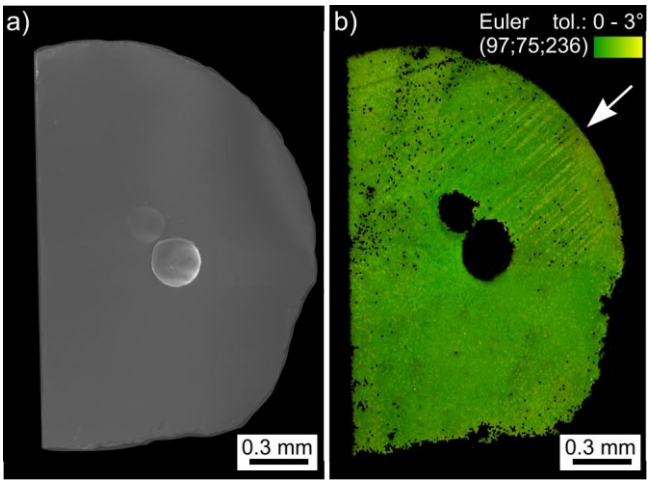

Figure 4: a) SEM-micrograph of the bead also featured in Figure 1 b). b) combined Orientation+IQ map of an EBSD-scan performed on the area.

After removing the mounting resin, this sample was analyzed using static NMR, i.e. a bulk technique, in order to verify the possible single crystallinity indicated by the cross section featured in Figure 4. For a single crystalline sample, the static spectrum should reveal a number of NMR lines which correspond to the number of non-magnetically equivalent crystallographic sites. Furthermore, the position of each line depends on the orientation of the crystal with respect to the static magnetic field, and the area under the curve is proportional to the multiplicity of the site if quantitative conditions are assumed.

$La_2Ga_3O_{7.5}$ has 12 non-magnetically equivalent crystallographic sites with the same multiplicity [18]. Hence the static NMR spectrum of a single crystal should contain 12 signals (peaks in the spectrum). Figure 5 a) presents the static ^{71}Ga NMR spectra obtained for the respectively stated rotor pitches. They clearly show that this sample cannot be a single crystal due to the large number of signals. A rough count of the spectrum with a pitch of $\varphi_0+81°$ suggests more than thirty signals, i.e. more than 3 orientation domains within the analyzed sample. Figure 5 b) could be used to allow a fine count, confirming the low number of

orientation domains [10,20], but this is beyond the scope of the work presented here as the true number of grains is irrelevant. In any case, these static spectra notably differ from that acquired from the powder, confirming a small number of orientation domains in the analyzed sample. As expected, the spectrum acquired from the powder is similar to that representing the sum of 180 pitches.

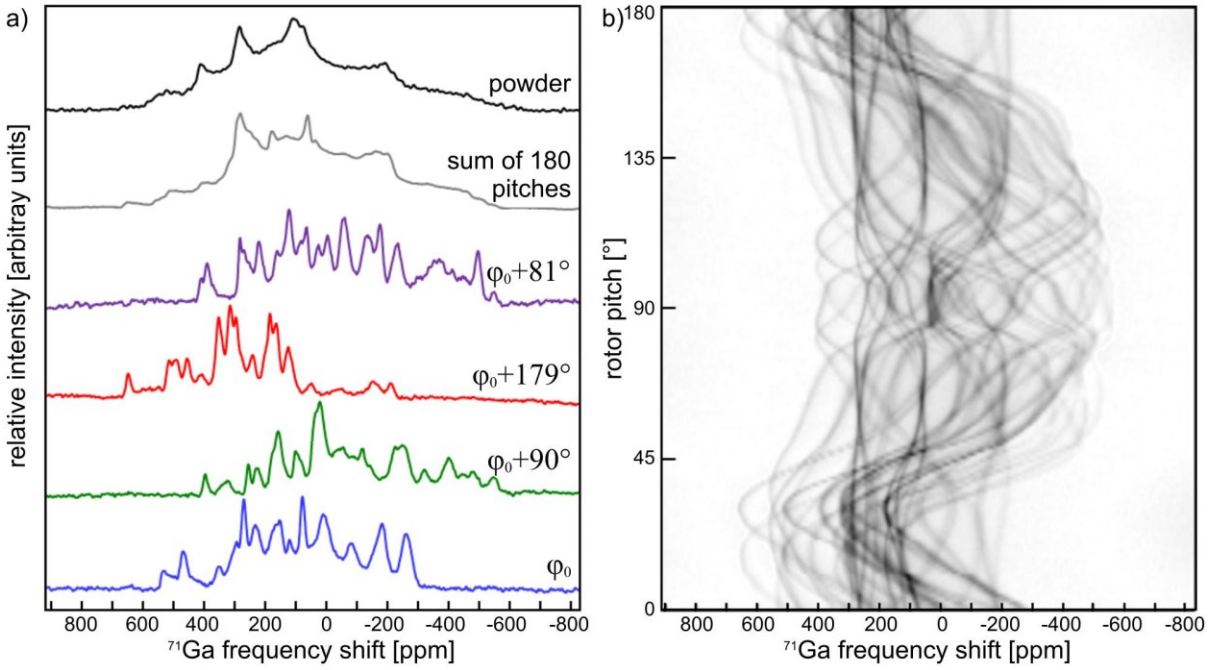

Figure 5: a) ^{71}Ga NMR spectra obtained from the sample featured in Figure 4 under static conditions at the respectively stated rotor pitches. The sum of the spectra over the 180 pitches is also presented as well as the spectrum acquired after powdering the sample. b) 2D map illustrating the ^{71}Ga spectrum as a function of the rotor pitch.

The crystallization of a bead containing only a few orientation domains, or ideally a single crystal, from a melt can only occur at temperatures close to the melting point as the nucleation rate must be very low. In the case of levitation melting, the lack of contact to a crucible ideally prevents heterogeneous nucleation sites, allowing a high level of undercooling after the heat sources are turned off. Nevertheless, dust particles in the air flow could lead to heterogeneous nucleation at the surface of the bead.

This leaves only two routes for the crystallization process: i) heterogeneous nucleation of the

melt by e.g. dust particles in the air flow while the melt is still too hot for homogeneous nucleation or ii) homogeneous nucleation in a severely undercooled melt. Here the first nucleus to form would ideally lead to a very fast crystallization of the melt, as supported by the frequently observed "crystallization flash" [12]. In both cases, nucleation is a localized event caused either an external heterogeneity or a cold spot in the melt.

The fast crystal growth necessary to produce a single crystal in the given experimental setup can only occur if the melt is severely undercooled, as the release of crystallization energy at the growth front would otherwise severely slow crystal growth, allowing time for further nucleation. Table 1 shows that a temperature spike of 318 K may occur while cooling a comparable sample, measured using a pyrometer. In the case of crystallizing Ba-fresnoite in a melt via electrochemically induced nucleation, a temperature spike of more than 80 K was measured as the growth front passed a thermocouple inserted into the melt [2]. Such thermal fields can potentially re-melt any secondary nuclei as they pass through a melt.

In order to increase the probability of a single nucleation event causing flash crystallization, the undercooling temperature must be maximized and nucleation events must be minimized. Measures towards this could be: using clean room conditions and cleaned gasses to minimize the chance of heterogeneous nucleation due to particles, using cooled gasses for levitation during cooling or optimizing the laser array so as to introduce a controlled "cold spot" on the melt sphere. The latter would locally trigger nucleation while most of the melt is too hot for nucleation but cold enough for crystal growth, similar to the process of electrochemically induced nucleation [21-23].

Figure 6 a) presents an SEM-micrograph of a cross section through the opaque sample presented in Figure 1 c) produced by protocol 2. While the SEM-micrograph implies a large number of grains, the combined IPF+IQ map of an EBSD-scan performed on the area shows

that the orientation domains are much larger, indicating that these crystals are dendrites and connected outside of the current cross section. A material file for $LaGaO_3$ based on ICSD file 50388 was used for indexing the EBSD-patterns in this scan. The crystallization of the sample is inhomogeneous as relatively large, dark areas providing no indexable EBSD-patterns are discernible. Pores of varying sizes occur in the sample, one is highlighted by the white arrow. The framed area is presented in greater detail in Figure 6 b) to highlight the irregular feature of dark contrast in the SEM-micrograph. EDXS-maps of c) La and d) Ga obtained from this region show that the bright, dendritic structures are enriched in La while Ga is accumulated in the interdendritic spaces and the area of dark contrast. 11 EDXS-spot measurements were acquired from the large dendritic crystals, the average at% composition is 20.1 Ga • 19.9 La • 60.0 O, i.e. a good agreement with the ideal composition of $LaGaO_3$. Measuring the composition of the residual glass or the lamellae is impossible as the information volume of EDXS in the SEM is in the µm-scale.

Figure 6 e) presents an SEM-micrograph of a larger pore partially filled with polishing media (bottom). The dendritic morphologies discernible at the inner surface of this pore adjacent to the prepared cross section provide a 3D-impression of the microstructure and confirm the growth mechanism of these crystals.

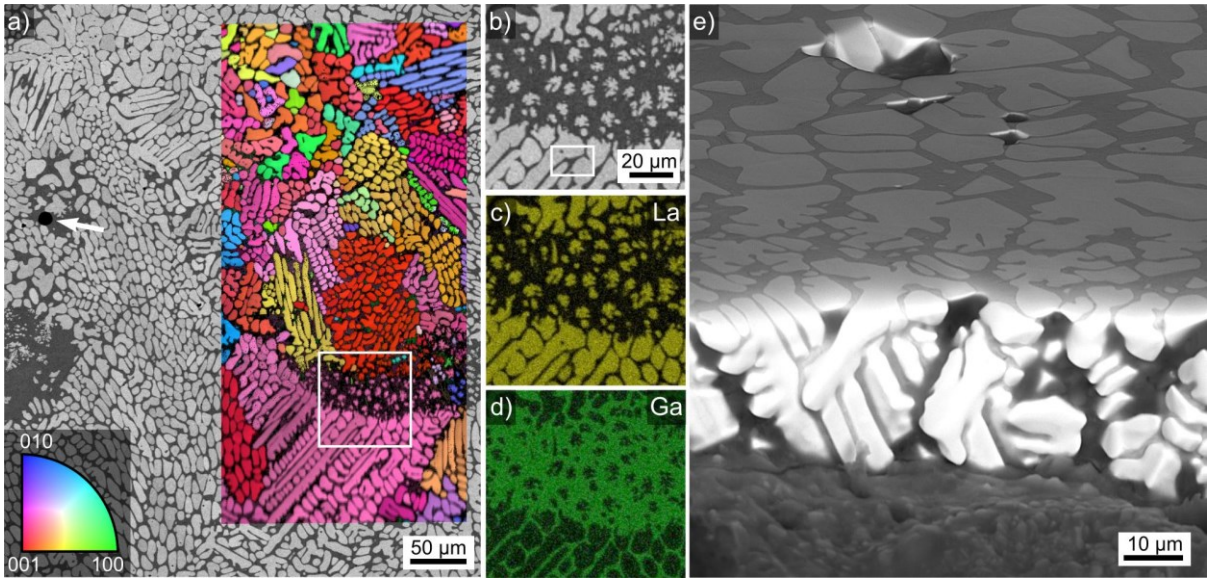

Figure 6: a) IPF+IQ-map of an EBSD-scan superimposed onto an SEM-micrograph of a cross section through the opaque sample. The white arrow highlights the location of a pore. b) SEM-micrograph of the framed area in a) presented in greater detail. The framed area here is described in further detail in Figure 7. EDXS-maps of this area are presented below illustrating the relative content of c) La and d) Ga. e) SEM-micrograph featuring the inner surface of a large pore adjacent to the prepared cross section.

The area framed in Figure 6 b) is presented in greater detail in Figure 7 a) with the IPF+IQ-map of an EBSD-scan performed on this area superimposed onto the SEM-micrograph. While the SEM-micrograph already implies crystalline, lamellar structures in-between the bright dendritic crystals, the IPF+IQ-map confirms this impression: reliably indexable EBSD-patterns are acquired from this area and they generally show that this crystal lattice shows the crystallographic orientation of the dendrites. A few areas show orientations deviating from this dominant orientation, one is circled in white. The framed area is presented in Figure 7 b) to illustrated the interdendric microstructure in greater detail. While both the lamellar microstructure and the orientational link to the dendritic structures show a remarkable similarity to the microstructure of Ba-fresnoite grown via electrochemically induced nucleation [21-23], the layer of honey-comb structures between the dendrites and the lamellae observed for Ba-fresnoite [22] does not occur in Figure 7 b). The area circled in white again marks as area providing EBSD-patterns different from those obtained from the dominant crystal lattice. It is noteworthy that most of the area of dark contrast in Figure 6 b) and enriched in Ga is composed of the lamellar crystallization, indicating this region showed a different chemical composition to most of the sample before crystallizing. Such slight chemical inhomogeneities can have a severe effect on crystal growth as e.g. illustrated for the growth of YAG at the boundary to a stria where the growth mechanism of YAG lattice changed from dendritic to polygon with the same crystal [24]. They can also serve to trigger nucleation and must be avoided when attempting to produce homogeneous beads.

EBSD-pattern I illustrates the excellent EBSD-pattern quality obtainable from the dendritic

$GaLaO_3$ lattice. Pattern II was obtained from the interdendritic crystallization. While it basically matches pattern I, it is of lower quality because some of the information volume contributing to this pattern is occupied by residual glass as the crystalline structures are so small. EBSD-pattern III was acquired from the area circled in white and clearly does not match the dominant crystal lattice, although trances from the latter are discernible. This EBSD-pattern superpositioning means that some of this dominant lattice was in the information volume contributing to pattern III. While some of the patterns in this area were indexed as $LaGaO_3$ but with a different orientation, pattern III also shows somewhat wider Kukichi bands than the patterns I and II.

The orientation homogeneity between the dendritic lattice and the interdendritic crystallization proves that the interdenritic crystals do not originate from independent nucleation but rather form during a secondary step of crystallization. While pattern III may have originated from an independent nucleation of $GaLaO_3$, this seems rather unlikely considering the otherwise connected crystal lattice of $GaLaO_3$. The somewhat broader Kikuchi lines and elevated level of Ga in these interdendritic spaces raise the question whether this pattern originates from a secondary phase, such as e.g. GeO_2, that crystallized in the residual glass. However, identifying this phase necessitates the use of TEM due to its small size and minimal occurrence.

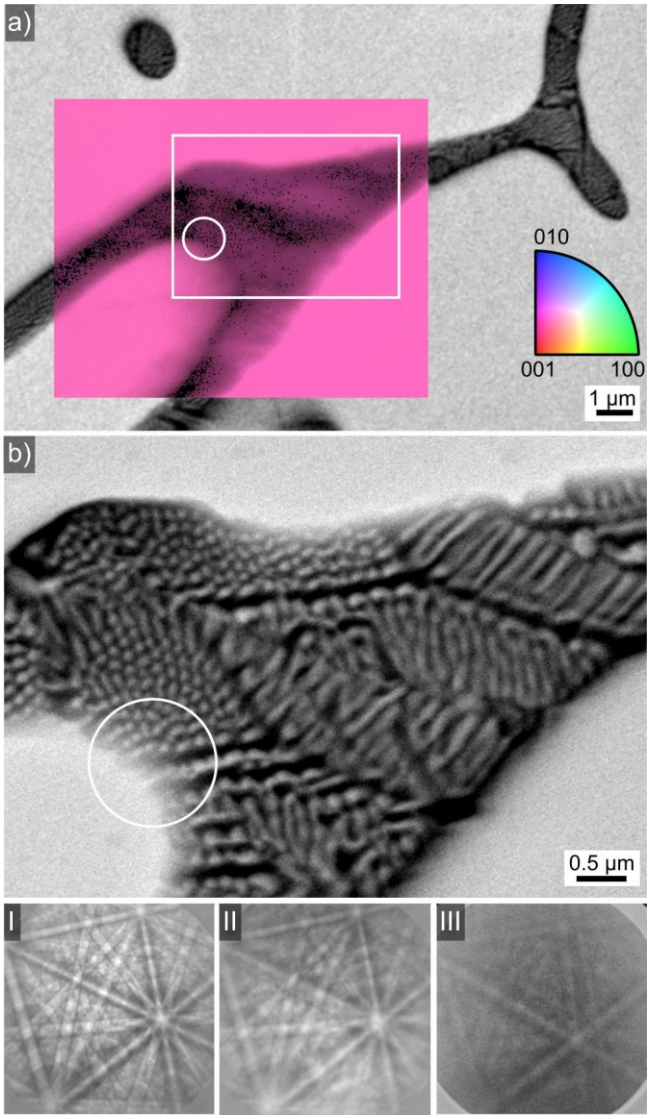

Figure 7: The area framed in Figure 6 b) in greater detail: a) IPF+IQ-map of an EBSD-scan superimposed onto an SEM-micrograph featuring a compact dendrite (bright) and the interdendritic crystallization. An area with a deviating orientation is circled in white. The framed area is presented in greater detail in b) via an SEM-micrograph where the area is again circled. EBSD-pattern I was acquired from the compact dendrite, pattern II from the interdendritic space and pattern III from the area circled in white.

Correlating the data in Table 1 with the phases and microstructures detected in the analyzed samples enables some conclusions concerning the cooling curves presented in Figure 2. First, however, a few assumptions must be made to reduce the number of parameters: (i) all melted beads have a comparable mass, (ii) although heavier gases (Ar vs. O) lead to a slower cooling of the sample, this is not significant to the performed experiments and (iii) the crystallization

enthalpies of $La_2Ga_3O_{7.5}$ and $LaGO_3$ (currently unknown) do not differ enough too significantly affect the experiments.

If these assumptions are correct, it is probable that the comparable temperature increase in the curves a) and b) result from the full crystallization of the respective beads while curve c) results from the only partial crystallization during dendritic growth. Analyzing the area under the curve to estimate the energy release during crystallization is not applicable as the experiment was not performed in a bomb calorimeter. The fast temperature increase in curve a) should result from the extremely fast crystal growth during flash crystallization in a severely undercooled melt. Nucleation throughout the bulk (curve b) would be slower, but still lead to a faster crystallization of the entire bead than dendritic growth (curve c). While the latter should show a faster growth velocity than polygon growth, the much smaller number of nucleation sites, which grow to a large size while being hindered by thermal and chemical diffusion, may lead to a relatively slow overall release of the crystallization energy.

The very fast cooling in curve a) may be attributed to the much faster thermal conduction in only a few orientation domains: if each grain has contact to the surface, each domain functions as a cooling single crystal. The slow cooling for curve c) is probably cause by the residual glass which generally shows a much slower thermal conduction than crystals.

In summary, the experiments presented above illustrate the potential to produce single crystals via aerodynamic levitation melting. Furthermore, they enable a wide range of hypotheses and experimental modifications for future work.

4. Conclusions

Crystallization after levitation melting can lead to multiple growth mechanisms and various nucleation rates. The microstructure can probably be identified by evaluating the cooling

curves recorded during crystallization, i.e. if the cooling curve does not match the expectation, the bead can be directly remelted allowing a very fast process restart. Levitation melting enables a higher level of process control than e.g. flame synthesis, but there are still many steps to take until it can be considered to be truly controlled.

While the crystallization of dendritic or polycrystalline microstructures has been known to occur, the comparably huge orientation domain proven in Figure 4 can been seen to prove that it should be possible to produce single crystals using levitation melting if the conditions for flash crystallization can be supplied. This would enable to produce single crystals of e.g. metastable phases and in turn measure their properties using optimal samples, even if they are of limited size. Modifications to push the process towards flash crystallization are proposed and it is clear that a close to perfect chemical composition of the melt is essential in order to achieve single crystals.

Corresponding Author

* *Wolfgang Wisniewski, Wolfgang.w@uni-jena.de*

Author Contributions

The manuscript was written through contributions of all authors. W. W. performed the EBSD results. M. J. P. and M.M acquired the cooling curves and provided theoretical background. E. V. obtained the SEM and EDXS results. J. F. produced the samples. V. S.-K. and F. F. acquired and evaluated the NMR data. All authors have given approval to the final version of the manuscript.

Funding Sources

Results incorporated in this paper have received funding from the European Union's Horizon 2020 research and innovation program under the Marie Skłodowska-Curie grant agreement No.

665790.

References

[1] Wisniewski, W.; Rüssel, C. Oriented Surface Nucleation in Inorganic Glasses - A Review, *Progr. Mater. Sci.* **2021**, 118, 100758.

[2] Wisniewski, W.; Thieme, K.; Rüssel, C. Fresnoite Glass-Ceramics – A Review, *Progr. Mater. Sci.* **2018**, 98, 68-107.

[3] Wisniewski, W.; Döhler, F.; Rüssel, C. Oriented Nucleation and Crystal Growth of Ba-Fresnoite ($Ba_2TiSi_2O_8$) in 2 BaO · TiO_2 · 2 SiO_2 Glasses with Additional SiO_2, *Cryst. Growth Des.* **2018**, 18, 3202-3208.

[4] Wisniewski, W.; Švančárek, P.; Prnová, A.; Parchovianský, M.; Galusek, D. Y_2O_3-Al_2O_3 Microsphere Crystallization Analyzed by Electron Backscatter Diffraction (EBSD), *Sci. Rep.* **2020**, 10, 11122.

[5] Prnová, A.; Karell, R.; Galusek, D. Al_2O_3–Y_2O_3 binary glass microspheres: synthesis and characterisation, *Adv. Mater. Res.* **2008**, 39-40, 189-192.

[6] Oran, W. A.; Berge, L. H. Containerless melting and solidification of materials with an aerodynamic levitation system, *Rev. Sci. Instrum.* **1982**, 53, 851-853.

[7] Nordine, P. C.; Weber, J. K. R.; Abadie, J. G. Properties of high-temperature melts using levitation, *Pure Appl. Chem.* **2000**, 72, 2127–2136.

[8] Lacy, L. L.; Robinson, M. B.; Rathz, T. J. Containerless undercooling and solidification in drop tubes, *J. Cryst. Growth* **1981**, 51, 47-60.

[9] Yoshimoto, K.; Masuno, A.; Ueda, M.; Inoue, H.; Yamamoto, H.; Kawashima, T. Low phonon energies and wideband optical windows of La_2O_3-Ga_2O_3 glasses prepared using an aerodynamic levitation technique, *Sci. Rep.*, **2017**, 7, 45600.

[10] Kuang, X.; Green, M. A.; Niu, H.; Zajdel, P.; Dickinson, C.; Claridge, J. B.; Jantsky, L.; Rosseinsky, M. J. Interstitial oxide ion conductivity in the layered tetrahedral network melilite structure, *Nature Mater.* **2008**, 7, 498-504.

[11] Boyer, M.; Yang, X.; Carrión, A. J. F.; Wang, Q.; Véron, E.; Genevois, C.; Hennet, L.; Matzen, G.; Suard, E.; Thiaudière, D.; Castro, C.; Pelloquin, D.; Kong, L. B.; Kuang, X.; Allix, M. First transparent oxide ion conducting ceramics synthesized by full crystallization from glass, *J. Mater. Chem. A*, **2018**, 6, 5276-5289.

[12] Fan, J.; Sarou-Kanian, V.; Yang, X.; Diaz-Lopez, M.; Fayon, F.; Kuang, X.; Pitcher, M. J.; Allix, M. $La_2Ga_3O_{7.5}$: A Metastable Ternary Melilite with a Super-Excess of Interstitial Oxide Ions Synthesized by Direct Crystallization of the Melt, *Chem. Mater.* **2020**, 32, 9016-9025.

[13] Boyer, M.; Carrion, A. J. F.; Ory, S.; Becerro, A. I.; Villette, S.; Eliseeva, S. V.; Petoud, S.; Aballea, P.; Matzen, G.; Allix, A. Transparent polycrystalline $SrREGa_3O_7$ melilite ceramics: potential phosphors for tuneable solid state lighting, *J. Mater. Chem. C* **2016**, 4, 3238-3247.

[14] Greca, M. C.; Emiliano, J. V.; Segadaes, A. M. Revised phase equilibrium relationships in the system Al_2O_3 ZrO_2 SiO_2, *J. Eur. Ceram. Soc.* **1992**, 9, 271–283.

[15] Wisniewski, W.; Otto, K.; Rüssel, C. Oriented Nucleation of Diopside Crystals in Glass, *Cryst. Growth Des.* **2012**, 12, 5035−5041.

[16] Harizanova, R.; Wisniewski, W.; Avdeev, G.; Rüssel, C.; Crystallization and growth morphology of barium titanate and fresnoite from a glass with the composition $20.1Na_2O{\cdot}23.1BaO{\cdot}23TiO_2{\cdot}9.8B_2O_3$ $\cdot 21SiO_2{\cdot}3Al_2O_3$, *CrystEngComm* **2017**, 19, 6208–6214.

[17] Wisniewski, W.; Saager, S.; Böbenroth, A.; Rüssel, C. Experimental evidence concerning the significant information depth of electron backscatter diffraction (EBSD), *Ultramicroscopy* **2017**, 173, 1-9.
[18] Vosegaard, T. Single-Crystal NMR Spectroscopy, *Progr. Nucl. Magn. Reson. Spectrosc.* **2021,** doi: https://doi.org/10.1016/j.pnmrs.2021.01.001.
[19] Vosegaard, T.; Hald, E.; Langer, V.; Skov, H. J.; Daugaard, P.; Bildsøe, H.; Jakobsen, H. J. Improved hardware and software for single-crystal NMR spectroscopy, *J. Magn. Reson.* **1998**, 135, 126–32.
[20] Xu, Y.; Bryce, D. L. SCFit: Software for single-crystal NMR analysis. free vs constrained fitting, *Solid State Nucl. Magn. Reson.* **2019**, 102, 53–62.
[21] Wisniewski, W.; Nagel, M.; Völksch, G.; Rüssel, C. New insights into the microstructure of oriented fresnoite dendrites in the system $Ba_2TiSi_2O_8$-SiO_2 through electron backscatter diffraction (EBSD), *Cryst. Growth Des.* **2010**, 10, 1939–1945.
[22] Wisniewski, W.; Nagel, M.; Völksch, G.; Rüssel, C. Irregular fourfold hierarchy in fresnoite dendrites grown via electrochemically induced nucleation of a$Ba_2TiSi_{2.75}O_{9.5}$ glass, *Cryst. Growth Des.* **2010**, 10, 4526–4530.
[23] Nagel, M.; Wisniewski, W.; Völksch, G.; Borschel, C.; Ronning, C.; Rüssel, C. Composition and texture of barium silicate crystals in fresnoite glass-ceramics by various scanning electron microscopic techniques, *CrystEngComm* **2011**, 13, 3383–3389.
[24] Keshavarzi, A.; Wisniewski, W.; Rüssel, C. EBSD and EDX Analyses of a Multiphase Glass-Ceramic Obtained by Crystallizing an Yttrium Aluminosilicate Glass, *ACS Appl. Mater. Interfaces* **2013**, 5, 8531−8536.

For Table of Contents Only

Macroscopic Orientation Domains grown via Aerodynamic Levitation - a Path towards Single Crystals

WolfgangWisniewski[1,2], Michael J. Pitcher[1], Emmanuel Veron[1], Jintai Fan[1,3], Vincent Sarou-Kanian[1], Franck Fayon[1] and Mathieu Allix[1]*

[1]CNRS, CEMHTI UPR3079, Univ. Orléans, F-45071 Orléans, France.

[2]Le Studium Research Fellow, Loire Valley Institute for Advanced Studies, Orléans & Tours, France.

[3]Chinese Academy of Science, Shanghai Institute of Optics and Fine Mechanics, Shanghai 201800, P. R. China.

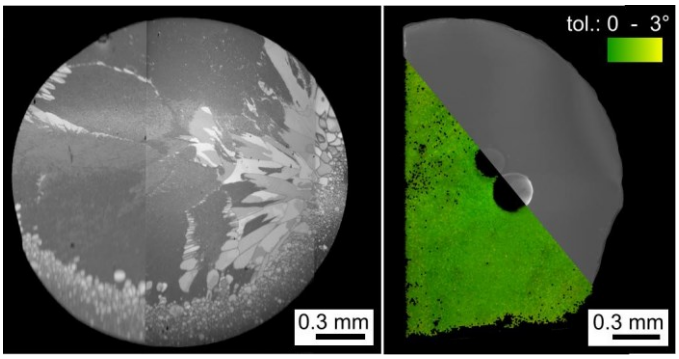

The levitated melt droplets crystallize to form $La_2Ga_3O_{7.5}$ or $LaGaO_3$ after the lasers are turned off. One of the beads containing $La_2Ga_3O_{7.5}$ shows a fully crystallized, polycrystalline microstructure. Another broke apart during cooling and its cross section shows only a single orientation domain which is more than 7 mm^2 in area. The bead containing $LaGaO_3$ showed dendritic growth.